An. Ştiinţ. Univ. Al. I. Cuza Iaşi. Mat. (N.S.)
Tomul LXVI, 2020, f. 2

Mathematical and numerical modeling of reentrant ventricular arrhythmias in the presence of Brugada syndrome

Silvia Caligari · Simone Scacchi

Abstract The Brugada syndrome (BrS) is a cardiac arrhythmic disorder responsible for sudden cardiac death associated with the onset of ventricular arrhythmias (VA), such as ventricular tachycardia and fibrillation. The mechanisms which lead to the onset of such electrical disorders in patients affected by BrS are not completely understood, yet. In a recent paper of 2018 by C. Pappone and collaborators, the authors have identified the presence of a region of cells with altered electrical properties (malignant VA substrate) in the right ventricle of BrS patients. Their experiments have shown that, when the malignant VA substrate is sufficiently large, conduction block of the excitation wavefront might occur, generating a ventricular arrhythmia. The aim of the present computational study is to validate in silico the results of these clinical experiments. To this end, we perform three-dimensional numerical simulations on an idealized wedge of human right-ventricular tissue, based on the Monodomain equations coupled with the ten Tusscher–Panfilov membrane model. In the malignant VA substrate, we have modified the maximal conductances of fast sodium current I_{Na}, L-type calcium current I_{CaL}, outward potassium current I_{to} and the intracellular conductivity coefficients, according to previously published data. The results have shown that the prolongation of action potential duration and the reduction of conduction velocity in the malignant VA substrate facilitate conduction blocks of activation wavefronts elicited by premature beats, yielding the onset of reentrant excitation.

Keywords Bidomain and Monodomain models · parallel numerical simulations · Brugada syndrome · ventricular arrhythmia · cardiac reentry

Mathematics Subject Classification (2010) MSC 65M22 · MSC 65M60 · MSC 65Z05

1 Introduction

The Brugada Syndrome (BrS), first described as a new clinical entity in [6], has attracted great interest because of its association with high risk of sudden cardiac death and susceptibility to ventricular arrhythmias (VA); see [2,3,5]. The mechanisms underlying the onset of such arrhythmic events in patients affected by BrS remain poorly understood.

Recent studies in selected patients with BrS have described complex arrhythmic substrates in the right ventricular outflow. The development of our

work has been inspired by a recent research published by C. Pappone and colleagues ([21]), who explored clinical and electrophysiological predictors of malignant ventricular tachyarrhythmia inducibility in BrS. In particular, they investigated the correlations between the presence and extent of a region of cells with altered electrical properties (malignant VA substrate) in the right ventricle of BrS patients and the pathophysiological basis of lethal VA, which remain still unclear.

Because of the limitation to experimental research involving human cardiac tissue, alternative methods such as computer modeling are of great interest, see [9,18,27,31]. Most previous simulation studies of BrS were mainly based on animal cell models and provided good references, but animal hearts, used for simulation studies, may differ significantly from human hearts. Therefore there is a need to use human cell models to investigate the electrophysiological mechanism of BrS.

The aim of the current study is to perform three-dimensional numerical simulations of reentrant arrhythmias in human right ventricular tissue in order to provide a theoretical support to the findings reported in [21], characterizing the electrical substrate in patients with BrS.

The quantitative models of cardiac cells serve the purpose of reproducing the details of the action potential shape while attempting to give reasonable mechanistic explanations of their behaviour. The difficulty with cardiac cells is that there are many different cell types and different types of ionic channels. For example, in the ventricles, epicardial, midmyocardial and endocardial cells have noticeable differences in action potential. Although it is not easy to represent the fine structure and connections between the cellular membrane and the intra and the extracellular spaces, it is possible to derive a macroscopic model by a homogenization process.

The result is a model of cardiac electrical activity called Bidomain Model. It consists of a degenerate parabolic system of two reaction-diffusion partial differential equations (PDEs), describing the spatio-temporal evolution of the the intra- and the extracellular electric potential in the cardiac muscle, coupled with a system of ordinary differential equations (ODEs) which describe the ionic currents. Because of the high computational costs required by the solution of the Bidomain system, we consider the simplified Monodomain model, which describes only the evolution of the transmembrane electric potential. There are several different techniques to speed up the numerical approximation of these models but in this work it is used a space discretization based on structured hexahedral isoparametric Q_1 finite elements and a semi-implicit finite-difference method in time.

The rest of the paper is organized as follows. In Sect. 2 we briefly review a membrane model for ionic currents and the Bidomain Model. In Sect. 3 we write the Bidomain and the Monodomain in a variational formulation followed by the discretization in space and time. In Sect. 4 we present our numerical results describing the geometrical domain considered and the calibration of channels conductivities and intercellular coupling in order to model the pathophysiology and ionic mechanisms of BrS.

2 Mathematical models

2.1 Mathematical models of human ventricular cells

Models of the ionic currents through the cardiac cellular membrane based on the Hodgkin-Huxley formalism ([17]) have been developed for the ventricular action potential, see [19,12]. The ionic current through channels of the membrane is modulated by the transmembrane potential v, the gating variables $w := (w_1, \dots, w_m)$ and the ionic concentration variables $c := (c_1, \dots, c_q)$. According to the Hodgkin-Huxley formalism, the ionic current has the following general structure

$$I_{ion}(v, w, c) = \sum_{k=1}^{n} G_k(v, c) \prod_{j=1}^{m} w_j^{p_{j_k}} (v - v_k(c)) + I_n(v, w, c),$$

where n is the number of ionic currents, G_k is the membrane conductance and v_k the reversal potential for the k^{th} current, p_{j_k} are integers and I_n accounts for time independent ionic fluxes. The dynamics of the gating variables w is described by a system of ODE's having the following structure

$$\begin{cases} \dfrac{dw_j}{dt} = R_j(v, w) = \alpha_j(v)(1 - w_j) - \beta_j(v) w_j \\ w_j(0) = w_{j,0} \\ \alpha_j, \quad \beta_j > 0, \quad 0 \le w_j \le 1, \quad j = 1, ..., m. \end{cases}$$

The dynamics of the ionic concentration variables c is described by the additional system of ODE's

$$\begin{cases} \dfrac{dc_j}{dt} = S_j(v, w, c) = -\dfrac{I_{c_j}(v, w) \cdot A_{cap}}{V_{c_j} \cdot z_{c_j} \cdot F} \\ c_j(0) = c_{j,0}, \quad j = 1, ..., q. \end{cases}$$

where I_{c_j} is the sum of ionic currents carrying ion c_j, A_{cap} is the capacitive membrane area, V_{c_j} is the volume of the compartment where c_j is updated, z_{c_j} is the valence of ion c_j and F is the Faraday constant The transmembrane current I_m is the sum of the capacitive current, related to the membrane lipidic bilayer, and of the ionic current I_{ion}. Since I_m must balance the applied current I_{app}, then the evolution of the TAP of a single myocyte is given by the following system of ODE's

$$\begin{cases} C_m \dfrac{dv}{dt} + I_{ion}(v, w, c) = I_m = I_{app}, \\ \dfrac{dw}{dt} - R(v, w) = 0, \quad \dfrac{dc}{dt} - S(v, w, c) = 0, \\ v(0) = v_0, \quad w(0) = w_0, \quad c(0) = c_0, \end{cases} \tag{2.1}$$

where C_m, I_{ion}, I_{app} are the surface capacitance, the ionic current of the membrane and the applied current per unit area of the membrane surface, respectively.

In the present study, we adopt a mathematical model of the action potential of human ventricular cells proposed in [25,26], the so-called ten Tusscher-Panfilov (TP06) model, which includes a high level of electrophysiological detail and it is enough computationally cost-effective to be applied in large-scale spatial simulations for the study of reentrant arrhythmias.

2.2 Mathematical models of ventricular tissue

The most complete mathematical model of the cardiac bioelectrical activity is the Bidomain model. It was first proposed in [28,16] and it is now the generally accepted model for the bioelectrical behavior of the cardiac tissue. This model consists of two degenerate parabolic reaction-diffusion equations describing the intra- u_i and the extracellular u_e potential in the cardiac muscle, coupled with a system of ordinary differential equations describing the ionic currents flowing through the cellular membrane. At the microscopic level, a model for the cellular structure of the cardiac tissue is complicated by the fact that the membrane potential, the intra- and the extracellular spaces are continuously connected and intertwined. It is difficult to write equations that take into account the fine structure of the geometry of these spaces. However it is possible to derive, by a homogenization process, a macroscopic model describing the averaged intra and extracellular electric potential and currents; for further details, we refer to [20,19,15,22]. On the well-posedness of the Bidomain model, we refer to [29,7].

Let $\Omega \subset \mathbb{R}^3$ be the bounded physical region occupied by the cardiac tissue. The intra- and the extracellular media are characterized by the conductivity tensors D_i and D_e. Because of the anisotropic structure, the conductivity is related to the arrangement of the cardiac fibers, whose direction rotates counterclockwise from epicardium to the endocardium. It is now possible to identify three distinct principal axes at any point $\mathbf{x}$. Let $\mathbf{a}_l(\mathbf{x})$, $\mathbf{a}_t(\mathbf{x})$ and $\mathbf{a}_n(x)$ be a triplet of orthonormal vectors related to the structure of the myocardium at a point $\mathbf{x}$, with $\mathbf{a}_l(\mathbf{x})$ parallel to the local fiber direction and $\mathbf{a}_t(\mathbf{x})$ normal to the muscle sheet. Let $\sigma_l^{i,e}$, $\sigma_t^{i,e}$, $\sigma_n^{i,e}$ be the conductivity coefficients measured along the corresponding directions. In general, these coefficients may depend on $\mathbf{x}$, but we assume they are constant, i.e. we are considering homogeneous anisotropy. Then the conductivity tensors, dependent on $\mathbf{x}$, are given by:

$$D_{i,e}(\mathbf{x}) = \sigma_l^{i,e}\mathbf{a}_l(\mathbf{x})\mathbf{a}_l^T(\mathbf{x}) + \sigma_t^{i,e}\mathbf{a}_t(\mathbf{x})\mathbf{a}_t^T(\mathbf{x}) + \sigma_n^{i,e}\mathbf{a}_n(\mathbf{x})\mathbf{a}_n^T(\mathbf{x}) \tag{2.2}$$

Recalling (2.1), the total membrane current per unit volume is given by

$$i_m = \chi I_m = \chi\left(C_m\frac{\partial v}{\partial t} + I_{ion}\right) \tag{2.3}$$

where $v = u_i - u_e$ is the transmembrane potential, the coefficient χ is the ratio of membrane area per tissue volume, C_m is the surface capacitance

of the membrane and I_{ion} is the ionic current. Imposing the conservation of currents, i.e. the interchange between the two media must balance the membrane current flow per unit volume, we have:

$$\mathrm{div}\mathbf{J}_i = -\mathrm{div}\mathbf{J}_e = i_m \tag{2.4}$$

where $\mathbf{J}_{i,e} = -D_{i,e}\,\mathrm{grad}\,u_{i,e}$ are the intra and the extracellular current densities.

We are now able to introduce the equations of the Bidomain model. Given the intra- and extracellualar applied currents per unit volume $i^{i,e}_{app} : \Omega \times (0,T) \longrightarrow \mathbb{R}$, where $(0,T)$ is the time interval (usually it coincides with a heartbeat), and initial conditions $v_0 : \Omega \longrightarrow \mathbb{R}$, $w_0 : \Omega \longrightarrow \mathbb{R}^m, c_0 : \Omega \longrightarrow \mathbb{R}^q$, find the intra- and the extracellular electric potentials $u_{i,e} : \Omega \times (0,T) \longrightarrow \mathbb{R}$, the transmembrane potential $v = u_i - u_e$ and the gating and ionic concentrations variables $w : \Omega \times (0,T) \longrightarrow \mathbb{R}^m$, $c : \Omega \times (0,T) \longrightarrow \mathbb{R}^q$ such that

$$\begin{cases} \chi C_m \dfrac{\partial v}{\partial t} - \mathrm{div}(D_i \nabla u_i) + \chi I_{ion}(v,w,c) = i^i_{app} & \text{in } \Omega \times (0,T) \\ -\chi C_m \dfrac{\partial v}{\partial t} - \mathrm{div}(D_e \nabla u_e) - \chi I_{ion}(v,w,c) = -i^e_{app} & \text{in } \Omega \times (0,T) \\ \dfrac{\partial w}{\partial t} = R(v,w) & \text{in } \Omega \times (0,T) \\ \dfrac{\partial c}{\partial t} = S(v,w,c) & \text{in } \Omega \times (0,T) \end{cases} \tag{2.5}$$

We also assume that the cardiac tissue is insulated, therefore homogeneous Neumann boundary conditions are assigned on $\partial\Omega \times (0,T)$

$$\mathbf{n}^T D_i \nabla u_i = 0, \mathbf{n}^T D_e \nabla u_e = 0.$$

Initial conditions are assigned in Ω for $t = 0$

$$\begin{cases} v(\mathbf{x},0) = u_i(\mathbf{x},0) - u_e(\mathbf{x},0) = v_0(\mathbf{x}), \\ w(\mathbf{x},0) = w_0(\mathbf{x}), \\ c(\mathbf{x},0) = w_0(\mathbf{x}). \end{cases} \tag{2.6}$$

Adding the first two equations of the system, we have

$$-\mathrm{div}D_i \nabla u_i - \mathrm{div}D_e \nabla u_e = i^i_{app} - i^e_{app}.$$

Integrating on Ω and applying the divergence theorem we have the following condition for the system to be solvable:

$$\int_\Omega i^i_{app}\, dx = \int_\Omega i^e_{app}\, dx \tag{2.7}$$

Concluding, the electric potentials, u_i and u_e, in bounded domains are determined up to the same additive time-dependent constant, while v is uniquely determined. The usual choice consists of selecting this constant so that u_e has zero average on Ω

$$\int_{\Omega} u_e \, dx = 0.$$

A simplified cardiac tissue model is the anisotropic *Monodomain* system, a parabolic reaction-diffusion equation describing the evolution of the transmembrane potential coupled with an ionic model. This model has been widely used for three-dimensional simulations because of its lower computational cost. Following the derivation reported in [14], the Bidomain system reduces to the Monodomain system:

$$\begin{cases} \chi C_m \dfrac{\partial v}{\partial t} - \operatorname{div}(D \nabla v) + \chi I_{ion}(v, w, c) = i_{app} \text{ in } \Omega \times (0, T) \\ \dfrac{\partial w}{\partial t} = R(v, w) \qquad \text{in } \Omega \times (0, T) \\ \dfrac{\partial c}{\partial t} = S(v, w, c) \qquad \text{in } \Omega \times (0, T) \end{cases} \tag{2.8}$$

where $D = D_e(D_i + D_e)^{-1} D_i$ and $i_{app} = i^e_{app} \frac{\sigma^i_l}{\sigma^i_l + \sigma^e_l}$, with homogeneous Neumann boundary conditions for v and initial conditions for $v,\ w,\ c$.

In our simulations, we will adopt this simplified model, coupled with the TP06 membrane model, presented in the previous section.

3 Numerical methods

The Bidomain equations are computationally expensive because it is impossible to formulate a solution scheme without having to solve a large system of linear algebraic equations every time step, see [30, 24, 13, 12]. Therefore, many simulation studies have adopted the Monodomain model which allows to reduce significantly the computational costs. Several space and time discretization strategies have been proposed for such models. In this work, we adopt the numerical approximation strategy developed in [11], based on semi-implicit finite differences for time discretization and structured hexahedral isoparametric Q_1 finite elements for space discretization.

3.1 Variational Formulation and Mathematical Analysis

Let V be the Sobolev space $H^1(\Omega)$, where $\Omega \subset \mathbb{R}^3$ is the bounded physical region occupied by the cardiac tissue, and define by

$$\begin{aligned} (\varphi, \psi) &= \int_\Omega \varphi\psi, && \forall \varphi, \psi \in L^2(\Omega) \\ a_{i,e}(\varphi, \psi) &= \int_\Omega (\nabla\varphi)^T D_{i,e}(\mathbf{x})\nabla\psi, && \\ a(\varphi, \psi) &= \int_\Omega (\nabla\varphi)^T D(\mathbf{x})\nabla\psi, && \forall \varphi, \psi \in H^1(\Omega) \end{aligned} \tag{3.1}$$

the usual L^2-inner product and elliptic bilinear forms.

Now we can consider the variational formulation of the Monodomain model. Given $v_0 \in L^2(\Omega),\ w_0 \in L^2(\Omega)^m, c_0 \in L^2(\Omega)^q,\ i_{app} \in L^2(\Omega\times(0,T))$, find:

- $v \in W^{1,1}((0,T); V)$,
- $w \in W^{1,1}((0,T); L^2(\Omega)^m)$,
- $c \in W^{1,1}((0,T); L^2(\Omega)^q)$

such that

$$\begin{cases} \chi C_m \dfrac{\partial}{\partial t}(v(t), \varphi) + a(v(t), \varphi) + \chi(I_{ion}(v, w, c), \varphi) = (i_{app}, \varphi) & \forall \varphi \in V \\ \dfrac{\partial}{\partial t}(w(t), \psi) = (R(v(t), w(t)), \psi) & \forall \psi \in L^2(\Omega)^m \\ \dfrac{\partial}{\partial t}(c(t), \zeta) = (S(v(t), w(t), c(t)), \zeta) & \forall \zeta \in L^2(\Omega)^q \end{cases} \tag{3.2}$$

with initial conditions (2.6) on $v,\ w,\ c$.

Analogously, we can write the variational formulation of the Bidomain model as follows. Given $v_0 \in L^2(\Omega),\ w_0 \in L^2(\Omega)^m, c_0 \in L^2(\Omega)^q,\ i^{i,e}_{app} \in L^2(\Omega \times (0,T))$, find:

- $u_{i,e} \in W^{1,1}((0,T); V)$,
- $w \in W^{1,1}((0,T); L^2(\Omega)^m)$,
- $c \in W^{1,1}((0,T); L^2(\Omega)^q)$

such that

$$\begin{cases} \chi C_m \dfrac{\partial}{\partial t}(v(t), \varphi_i) + a_i(u_i(t), \varphi_i) + \chi(I_{ion}(v, w, c), \varphi_i) = (i^i_{app}, \varphi_i) & \forall \varphi_i \in V \\ -\chi C_m \dfrac{\partial}{\partial t}(v(t), \varphi_e) + a_e(u_e(t), \varphi_e) - \chi(I_{ion}(v, w, c), \varphi_e) = -(i^e_{app}, \varphi_e) & \forall \varphi_e \in V \\ \dfrac{\partial}{\partial t}(w(t), \psi) = (R(v(t), w(t)), \psi) & \forall \psi \in L^2(\Omega)^m \\ \dfrac{\partial}{\partial t}(c(t), \zeta) = (S(v(t), w(t), c(t)), \zeta) & \forall \zeta \in L^2(\Omega)^q \end{cases} \tag{3.3}$$

with initial condition (2.6) on $v,\ w,\ c$ and the compatibility condition (2.7) on $i^{i,e}_{app}$.

3.2 Finite Element Discretization in Space

Let the domain Ω be a three-dimensional slab of cardiac tissue. We discretize Ω by introducing a structured quasi-uniform grid of $n_i \times n_j \times n_k$ hexahedral isoparametric Q_1 finite elements. Applying the finite element approximation, we have $\Omega = \bigcup_{E \in \mathcal{T}_h} E$, where $E = T_E(\hat{E})$, with $\hat{E} = [-1, 1]^3$ and T_E is a trilinear map. The associate finite element space is given by

$$V_h = \left\{ \varphi_h \in V : \varphi_h \text{is continuous in } \Omega : \varphi_{h|E} \circ T_E \in Q_1(\hat{E}), \forall\ E \in \mathcal{T}_h \right\} \tag{3.4}$$

where $Q_1(\hat{E})$ is the space if the trilinear functions on $\hat{E}$. A semi-discrete problem can be obtained by applying a standard Galerkin procedure, see e.g. [23], and choosing a finite element basis $\{\varphi_i\}$ for V_h. Let $M = (m_{r,s}), A = (a_{r,s})$ and $A_{i,e} = (a^{i,e}_{r,s})$ be the symmetric mass and stiffness matrices defined by

$$\begin{aligned} m_{r,s} &= \sum_E \int_E \varphi_r \varphi_s dx \\ a_{r,s} &= \sum_E \int_E (\nabla \varphi_r)^T D(\mathtt{x}) \nabla \varphi_s dx \\ a^{i,e}_{r,s} &= \sum_E \int_E (\nabla \varphi_r)^T D_{i,e}(\mathtt{x}) \nabla \varphi_s dx \end{aligned}$$

Let $I^h_{ion}, I^h_{app}, I^{i,h}_{app}, I^{e,h}_{app}$ be the finite element interpolants of I_{ion}, i_{app}, i^i_{app}, i^e_{app} respectively.

In the Monodomain model, the finite element approximation v_h of the transmembrane potential is the solution of the semi-discrete system

$$\chi C_m M \frac{dv_h}{dt} + A v_h + \chi M I^h_{ion}(v_h, w_h, c_h) = M I^h_{app} \tag{3.5}$$

while in the Bidomain model, the finite element approximation $u_{i,h}, u_{e,h}$ of the intra- and extracellular potentials are the solution of the semi-discrete system

$$\begin{cases} \chi C_m M \dfrac{dv_h}{dt} + A_i u_{i,h} + \chi M I^h_{ion}(v_h, w_h, c_h) = M I^{i,h}_{app} \\ -\chi C_m M \dfrac{dv_h}{dt} + A_e u_{e,h} + \chi M I^h_{ion}(v_h, w_h, c_h) = M I^{e,h}_{app} \end{cases} \tag{3.6}$$

where $v_h = u_{i,h} - u_{e,h}$. In both cases, these equations are coupled with the semi-discrete approximations of the membrane model

$$\begin{cases} \dfrac{dw_h}{dt} = R(v_h, w_h) \\ \dfrac{dc_h}{dt} = S(v_h, w_h, c_h) \end{cases} \tag{3.7}$$

The Bidomain system can be written in compact form

$$\chi C_m \mathcal{M} \frac{d}{dt} \begin{bmatrix} u_{i,h} \\ \\ u_{e,h} \end{bmatrix} + \mathcal{A} \begin{bmatrix} u_{i,h} \\ \\ u_{e,h} \end{bmatrix} + \chi \begin{bmatrix} MI^h_{ion}(v_h, w_h, c_h) \\ \\ -MI^h_{ion}(v_u, w_h, c_h) \end{bmatrix} = \begin{bmatrix} MI^{i,h}_{app} \\ \\ MI^{e,h}_{app} \end{bmatrix} \tag{3.8}$$

where

$$\mathcal{M} = \begin{bmatrix} M & -M \\ -M & M \end{bmatrix}, \quad \mathcal{A} = \begin{bmatrix} A_i & 0 \\ 0 & A_e \end{bmatrix}$$

3.3 Semi-implicit Time Discretization

In the semi-implicit discretization in time, the reaction terms are treated explicitly while the diffusion terms implicitly. The ODE system for the gating and concentrations variables can be discretized by the semi-implicit Euler method

$$\begin{cases} \dfrac{w^{n+1} - w^n}{\Delta t} = R(v^n, w^{n+1}) \\ \dfrac{c^{n+1} - c^n}{\Delta t} = S(v^n, w^{n+1}, c^n) \end{cases} \tag{3.9}$$

Then we can obtain a solution for v^{n+1} in the Monodomain case

$$\chi C_m M \frac{v^{n+1} - v^n}{\Delta t} + A v^{n+1} + \chi MI^h_{ion}(v^n, w^{n+1}, c^{n+1}) = MI^h_{app} \tag{3.10}$$

or a solution for u_i^{n+1}, u_e^{n+1} in the Bidomain case

$$\begin{cases} \chi C_m M \dfrac{v^{n+1} - v^n}{\Delta t} + A_i u_i^{n+1} + \chi MI^h_{ion}(v^n, w^{n+1}, c^{n+1}) = MI^{h,i}_{app} \\ -\chi C_m M \dfrac{v^{n+1} - v^n}{\Delta t} + A_e u_e^{n+1} + \chi MI^h_{ion}(v^n, w^{n+1}, c^{n+1}) = MI^{h,e}_{app} \end{cases} \tag{3.11}$$

where $v^n = u_i^n - u_e^n$.
Alternatively, it is possible solving the potentials first, given the gating and the concentration variables at the previous time step, and then the new gating and concentration variables.

4 Numerical simulations

We report in this section the results of parallel numerical simulations of the three-dimensional slab of right ventricular tissue, performed on 40 cores of the Linux cluster Horizon of the Department of Mathematics of the University of Milan. The code is written in Fortran90 and is based on the parallel libraries MPI and PETSc [4], developed at the Argonne National Laboratory (USA).

4.1 Computational domain, discretization and tissue parameters

The geometric model considered consists of a three-dimensional slab of right ventricular tissue of size $5.76 \times 6.00 \times 0.36\ cm^3$. The domain is discretized by introducing a structured grid of $n_i \times n_j \times n_k$ hexahedral isoparametric Q_1 elements obtained by a uniform subdivision of the slab with a mesh size of $h = 1.5 \cdot 10^{-2}$ (cm), where

$$n_i = 384 \qquad n_j = 400 \qquad n_k = 24. \tag{4.1}$$

For the semi-implicit discretization in time we use a time step of $0.05\ ms$.

We also assume a transversely isotropic tissue with conductivity coefficients

$$\begin{aligned} &\sigma_l^e = 2 \times 10^{-3} \Omega^{-1} cm^{-1}, && \sigma_l^i = 3 \times 10^{-3} \Omega^{-1} cm^{-1} \\ &\sigma_t^e = 1.3514 \times 10^{-3} \Omega^{-1} cm^{-1}, && \sigma_t^i = 3.1525 \times 10^{-4} \Omega^{-1} cm^{-1} \\ &\sigma_n^e = \sigma_t^e, && \sigma_n^i = \sigma_t^i \end{aligned} \tag{4.2}$$

To model the malignant VA substrate, we introduce a region of cells, of size $2.88 \times 3.84 \times 0.36\ cm^3$ (see Fig. 4.1-top panel), where channels conductivities and intercellular coupling are modified according to BrS characteristic, described in the next sub-section.

4.2 BrS parameter setting

In the ECG waveforms, a coved ST segment elevation pattern followed by a negative T wave is considered diagnostic of the Brugada syndrome. A reduced function of cardiac sodium channel plays an important role in the mechanism of BrS: the sodium channel blockers can provoke or augment the Brugada ECG pattern and mutations in SCN5A, the gene encoding the α-subunit of the cardiac sodium channel, are identified in $\sim$20% of patients.

The disorder more frequently observed in mutations in SCN5A is a decrease of sodium current I_{Na} ([10]), which leads to an imbalance between the positive inward and outward currents at the end of the transient repolarization phase of the cell action potential. This imbalance should occur with decreases of inward sodium I_{Na} and L-type calcium I_{CaL} currents or an increase of outward potassium I_{to} current, which leads to a development of a characteristic notch and the loss of action potential dome. Thus, one of the way in which arrhythmias may occur in Brugada syndrome is through the formation of a heterogeneous substrate, in which a region exhibits abnormal action potentials. Such a substrate might be responsible for the onset of reentrant arrhythmias, as suggested in [21].

Following the approach of Hoogendijk et al. ([18]), where ST segment elevation is connected to reductions of sodium channel (G_{Na}) and L-type calcium channel (G_{CaL}) maximal conductances and an increase of potassium channel (G_{to}) maximal conductance, in our simulations, we modify in the

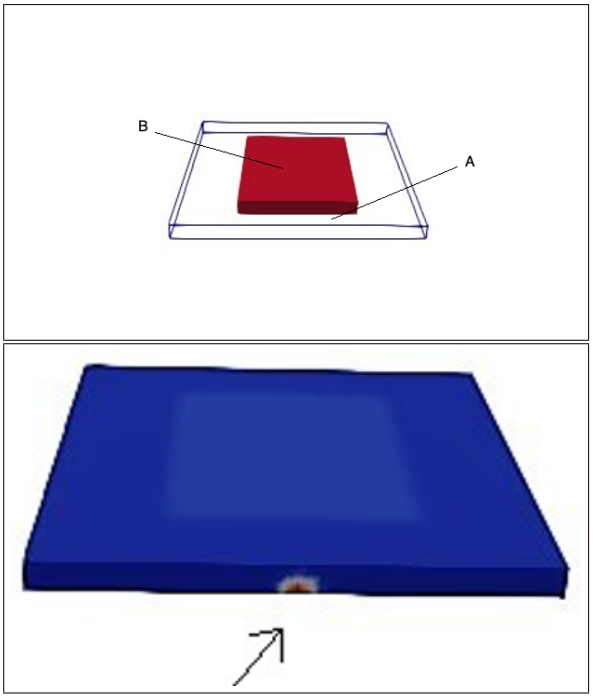

Fig. 1 Top: Three-dimensional slab of ventricular tissue. The red box represents the region of cells affected by Brugada syndrome (BrS). Bottom: area of the slab where the stimulus is applyed.

TP06 model G_{Na}, G_{CaL} and G_{to} in the region of BrS cells.
Referring to Antzelevitch ([1]), we also augment the slow delayed rectifier current conductivity G_{Ks} and the potassium external concentration K_o, trying to accentuate the action potential notch.

We consider the following different settings:

- **Slab 1**: G_{Na}, G_{CaL} and G_{to} are set in the BrS region at 20%, 70% and 150% of their normal values, respectively;
- **Slab 2**: in addition to the **Slab 1** conditions, the intracellular conductivity coefficients σ_l^i and σ_t^i are set in the BrS region at 25% and 12.5% of their normal values, respectively;
- **Slab 3**: G_{Na}, G_{CaL} and G_{to} are set in the BrS region at 20%, 70% and 300% of their normal values, respectively;
- **Slab 4**: in addition to the **Slab 3** conditions, σ_l^i and σ_t^i are set in the BrS region at 25% and 12.5% of their normal values, respectively;
- **Slab 5**: in addition to the **Slab 4** conditions, G_{Ks} and K_o are set in the BrS region at 70% and 120% of their normal values, respectively.

4.3 Stimulation protocol

Risk stratification in BrS is still challenging, especially in asymptomatic case. In general, patients with documented ventricular fibrillation should receive an implantable cardioverter defibrillator. However, for individuals with a typical BrS ECG without documented ventricular fibrillation, the best approch is still unclear. Pedro and Josep Brugada were the first to propose in 2002 ([8]), on the basis of data from their registry, that arrhythmia inducibility at programmed electrical stimulation (PES) could be useful to identify patients at high risk.

For our simulations we have decided to use the same pacing procedure introduced in [8]. The excitation process is started by applying a stimulus of 350 mA/cm^3 for 1 ms on a small area $0.12 \times 0.12 \times 0.06$ cm^3 at the base of the slab, see Fig. 4.1 (Bottom panel). For each simulation setting, we first apply four pacing stimuli (S1) at a basic cycle length (BCL) of 500 ms. Then, a premature stimulus (S2) is delivered 350 ms after S1. If S2 does not generate a re-entrant arrhythmia, the S1-S2 coupling interval is shortened in steps of 10 ms until arrhythmia is induced or the S2 fails to trigger excitation. If arrhythmia is not induced, an additional S3, and if necessary S4, is delivered in the same manner as S2 (initially delivered 350 ms after previous stimulus, and then shortened until arrhythmia is induced or the stimulus fails). The simulation of a single cardiac beat in this model required 3-4 hours.

4.4 Results and Discussion

4.4.1 Slab 1 and Slab 2 simulations

Fig. 2 reports the spatial distribution of transmembrane potential computed from the **Slab 1** simulation at eight time snapshots after an S2 stimulus applied at 300 ms later than the last S1 stimulus and an S3 stimulus applied at 240 ms later than S2. The excitation wavefront elicited by the S3 stimulus undergoes a conduction block when it reaches the bottom border of the BsR region (see Fig. 2-(B)), which is still refractory due to the prolongation of the action potential. Then excitation moves around the BsR region, entering it through the lateral borders (see Fig. 2-(C)) and thus inducing a cycle of reentry (see Fig. 2-(D-F)). However, the reentrant activation wavefront is not sustained, since excitation dies after the first cycle (see Fig. 2-(H)). Fig. 3 displays two action potential waveforms, computed at sites A and B of Fig. 4.1 (Top panel). Site A is in the normal tissue, whereas site B is in the BsR region. From these waveforms, it is clear that excitation dies after the first cycle of reentry.

Fig. 4 reports the spatial distribution of transmembrane potential computed from the **Slab 2** simulation at eight time snapshots. Even in this case, the S2 stimulus is delivered 300 ms later than the last S1 stimulus and

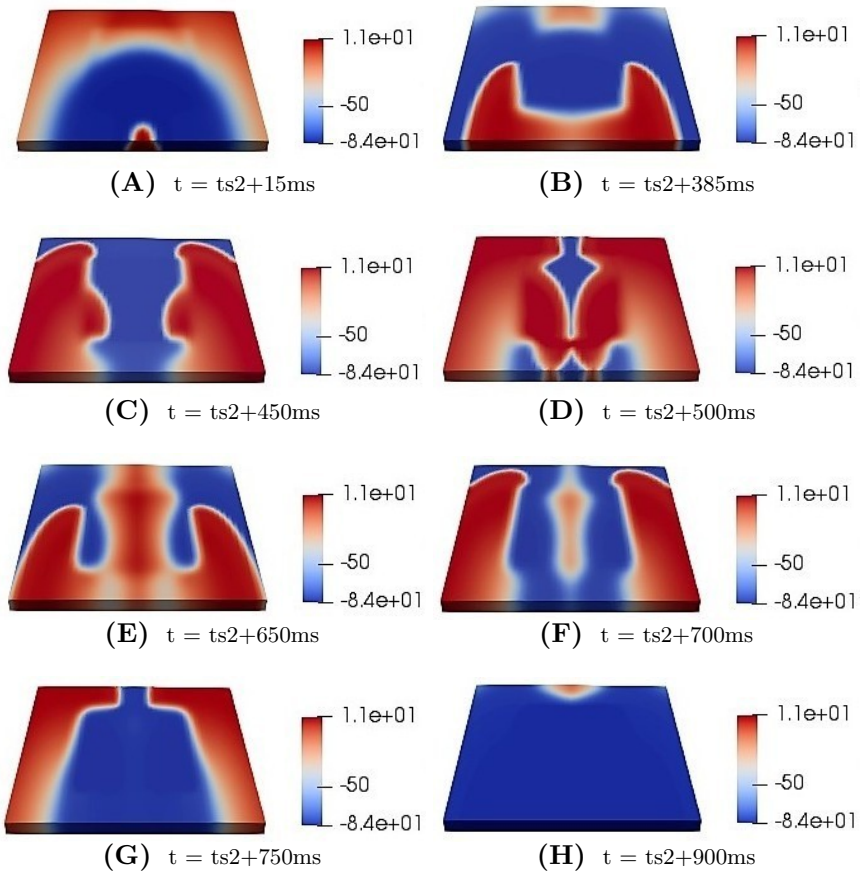

Fig. 2 Slab 1 simulation. Snapshots of transmembrane potential distributions at eight time instant after the S2 stimulus applied at $ts2 = 300\ ms$, being $t = 0$ the onset of the last S1 stimulus.

the S3 stimulus is applied 240 ms later than S2. The excitation wavefront elicited by the S3 stimulus is blocked when it reaches the bottom border of the BsR region (see Fig. 4-(B)) and it proceed along the lateral borders of the BsR region (see Fig. 4-(C)), re-exciting it entering then from the top border (see Fig. 4-(D)). Consequently, a reentrant excitation is generated, that remains sustained, as also confirmed by the action potential waveforms displayed in Fig. 4.4.

Thus, the reduction in the model of the intercellular coupling by modifying the intracellular conductivity coefficients in BrS region is fundamental in determining the maintenance of reentry.

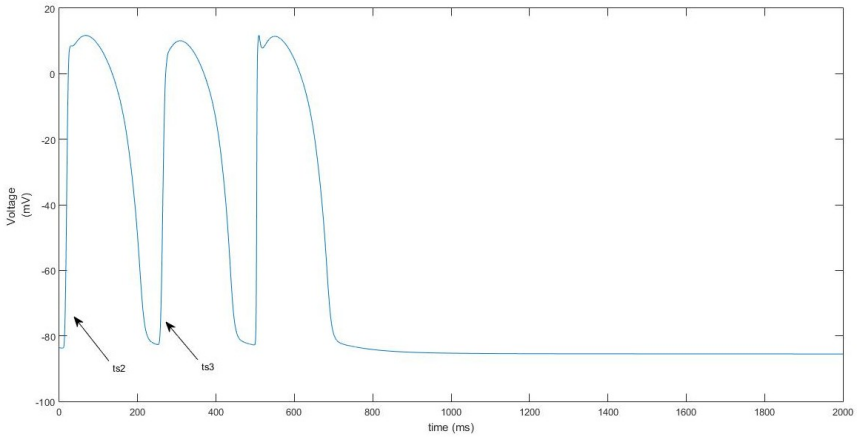

(A) Transmembrane action potential at point A in Fig. 4.1 (Top panel).

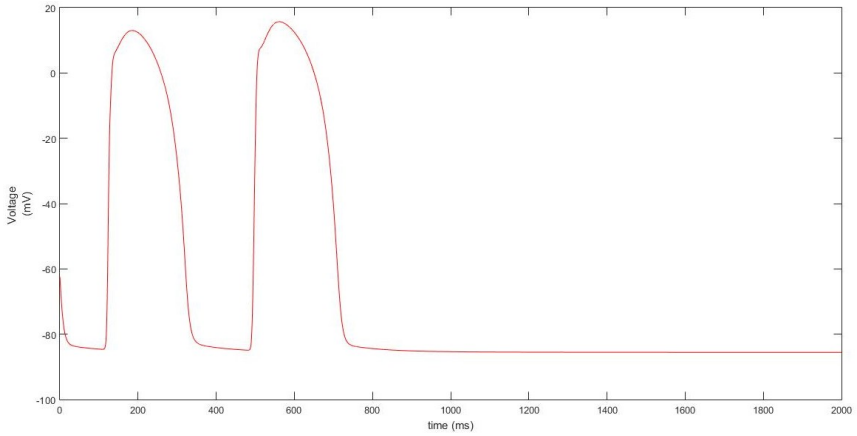

(B) Transmembrane action potential at point B in FIg. 4.1 (Top panel).

Fig. 3 Slab 1 simulation. Transmembrane action potential waveforms computed from two sites in the normal (A) and Brugada (B) cell regions.

4.4.2 Slab 3 and Slab 4 simulations

In the second set of simulations, we set the G_{to} maximal conductance in the BrS region at 300 % of the normal value, whereas the values of the other parameters are the same as in the previous tests. Fig. 6 reports the spatial distribution of transmembrane potential computed from the **Slab 3** simulation at eight time snapshots after an S2 stimulus applied at 300 ms later than the last S1 stimulus and an S3 stimulus applied at 240 ms later than S2. As it happens in the **Slab 1** simulation, after the S3 stimulus, one cycle of reentry occurs, due to the conduction block when the excitation wave-

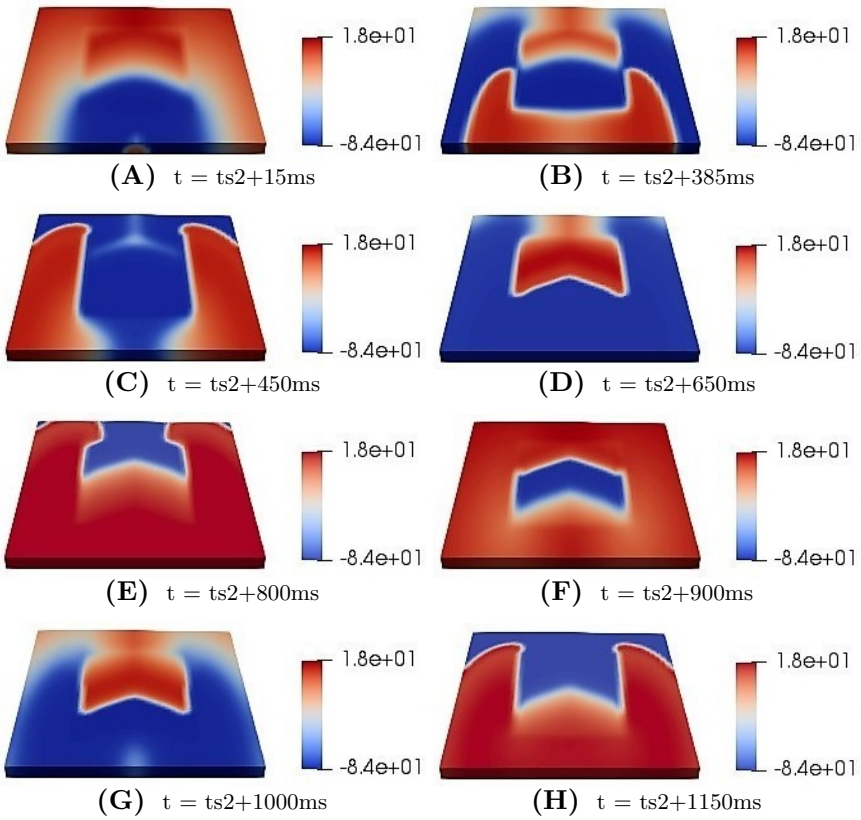

Fig. 4 Slab 2 simulation. Snapshots of transmembrane potential distributions at eight time instant after the S2 stimulus applied at $ts2 = 300\ ms$, being $t = 0$ the onset of the last S1 stimulus.

front reaches the bottom border of the BrS regions. However, the reentry is not sustained.

Then, in **Slab 4** simulation, we reduce the intracellular conductivity as done for **Slab 2**, keeping unchanged the other parameters. Fig. 7 reports the spatial distribution of transmembrane potential computed from the **Slab 4** simulation at eight time snapshots. Even in this case, the S2 stimulus is delivered 300 ms later than the last S1 stimulus and the S3 stimulus is applied 240 ms later than S2. The excitation wavefront originating from the S3 stimulus is blocked at the bottom border of the BrS region, moves around its lateral borders and then re-enter it from the top border, yielding a reentrant excitation, that remains sustained, as also confirmed by the transmembrane action potential waveforms displayed in Fig. 8. This result confirms that the reduction of intracellular conductivities, together with the

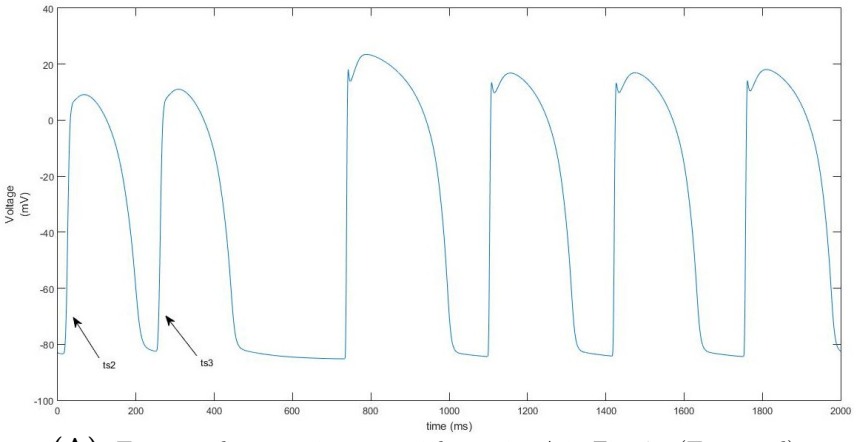

(A) Transmembrane action potential at point A in Fig. 4.1 (Top panel).

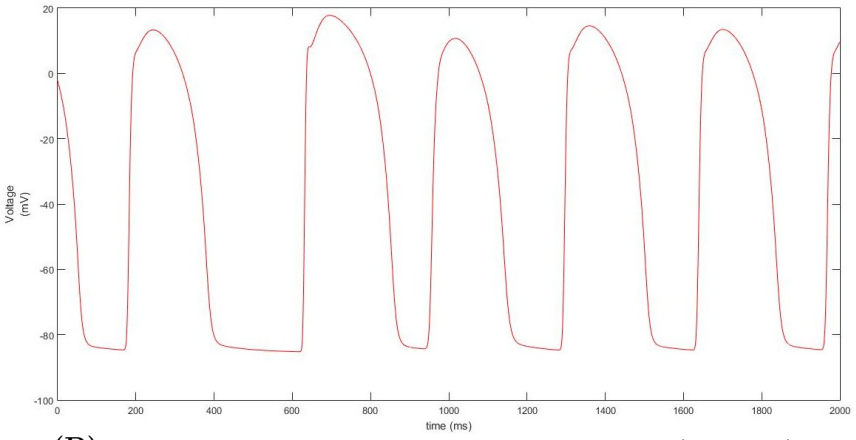

(B) Transmembrane action potential at point B in Fig. 4.1 (Top panel).

Fig. 5 Slab 2 simulation. Transmembrane action potential waveforms computed from two sites in the normal (A) and Brugada (B) cell regions.

modifications of G_{Na}, G_{CaL} and G_{to} conductances, determines the maintenance of the reentrant arrhythmia.

4.4.3 Slab 5 simulation

In the BrS region, we set the sodium channel conductivity G_{Na} at 20% of normal, calcium channel conductivity G_{CaL} at 70% of normal, potassium channel conductivity G_{to} at 150% of normal and we modify the slow delayed rectifier current conductivity G_{Ks} and potassium external concentration K_o. The first one is associated with the plateau phase of the action potential

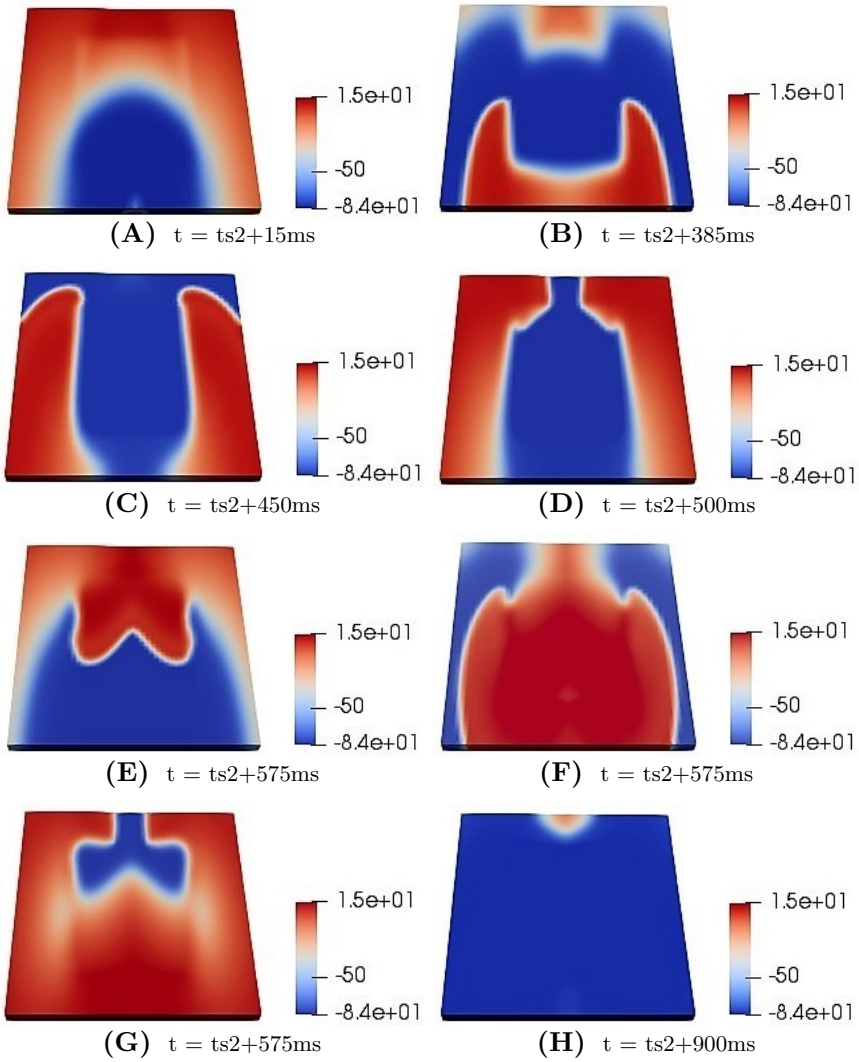

Fig. 6 Slab 3 simulation. Snapshots of transmembrane potential distributions at eight time instant after the S2 stimulus applied at $ts2 = 300\ ms$, being $t = 0$ the onset of the last S1 stimulus.

and its formulation is based on an activation gate and a reversal potential determined by a small permeability to sodium and a large permeability to potassium ions. The second one is connected to the fast repolarization phase. The G_{Ks} and K_o parameters are fixed at 70% and 120% of their normal

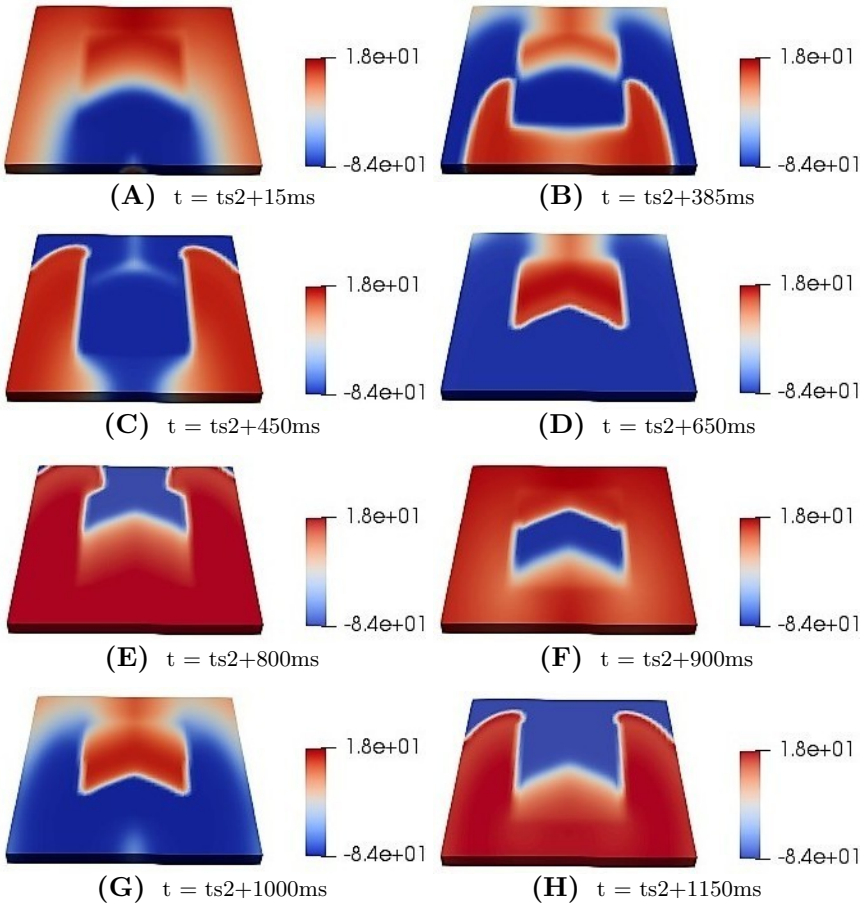

Fig. 7 Slab 4 simulation. Snapshots of transmembrane potential distributions at eight time instant after the S2 stimulus applied at $ts2 = 300\ ms$, being $t = 0$ the onset of the last S1 stimulus.

values, respectively. We also set the intracellular conductivity coefficients σ_l^i and σ_t^i at 25% 12.5% of the normal values.

Fig. 9 reports the spatial distribution of transmembrane potential computed at eight time snapshots. Even in this case, the S2 stimulus is delivered 300 ms later than the last S1 stimulus. The excitation wavefront originating from the S2 stimulus is blocked at the bottom border of the BrS region, moves around its lateral borders and then re-enter it from the top border, yielding one cycle of reentry. However, the reentry is not sustained.

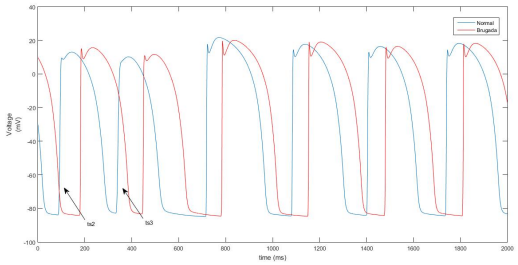

Fig. 8 Slab 4 simulation. Transmembrane action potential waveforms computed from two sites in the normal (A) and Brugada (B) cell regions.

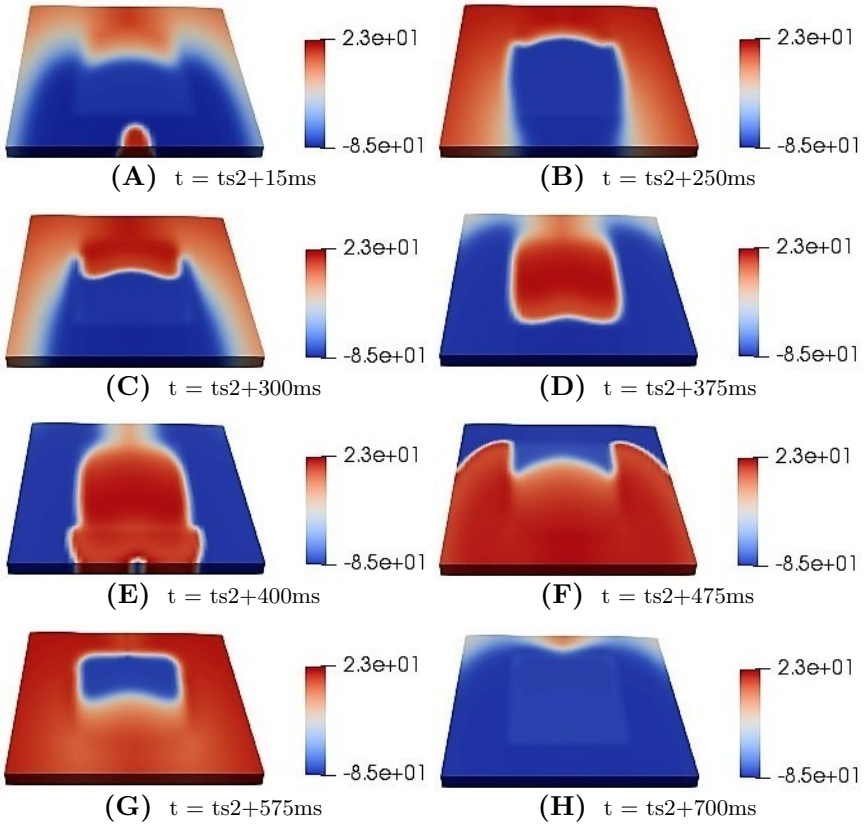

Fig. 9 Slab 5 simulation. Snapshots of transmembrane potential distributions at eight time instant after the S2 stimulus applied at $ts2 = 300\ ms$, being $t = 0$ the onset of the last S1 stimulus.

5 Conclusion

We have investigated by means of three-dimensional numerical simulations the mechanisms producing successful initiation of reentry in the presence of BrS. The mathematical model includes the Monodomain system for the bioelectrical current flow in the cardiac ventricular tissue, the transversely isotropic conductivities, the structure of the fiber architecture and the ten Tusscher-Panfilov membrane model. The parallel code is based on isoparametric Q_1 finite elements in space and a semi-implicit finite-difference method in time. Parallelization and portability are based on the PETSc parallel library. The results have shown that the combined role of conduction and repolarization abnormalities and the reduced electrical coupling is an important determinant for the initiation and maintenance of reentrant arrhythmias.

Acknowledgements S.C. and S.S. are grateful to INDAM-GNCS for support. S.S. was partially supported by grants of MIUR (PRIN 2017AXL54F_003).

References

1. Antzelevitch, C. – *Basics mechanism of reentrant arrhythmias*, Curr. Opin. Cardiol., **16** (2001), no. 1, 1-7.
2. Antzelevitch, C. – *The Brugada syndrome: ionic basis and arrhythmia mechanisms*, J. Cardiovasc. Electrophysiol., **12** (2001), no. 2, 268-272.
3. Antzelevitch, C. – *Brugada syndrome*, Pacing Clin. Electrophysiol., **29** (2006), 1130-1159.
4. Balay, S.; Abhyankar, S.; Adams, M.; Brune, P.; Buschelman, K.; Curfman McInnes, L.; Dalcin, L.; Gropp, W.; Karpeyev, D.; Kaushik, D.; Knepley, M.; Rupp, K.; Smith, B.; Zampini, S.; Zhang, H.; Zhang, H. – *PETSc users manual*, Tech. Rep. ANL-95/11 - Revision 3.7, Argonne National Laboratory, 2016.
5. Benito, B.; Brugada, J.; Brugada, R.; Brugada, P. – *Brugada syndrome*, Rev. Esp. Cardiol., **62** (2009), no. 11, 1297-1315.
6. Brugada, P.; Brugada, J. – *Right bundle branch block, persistent ST segment elevation and sudden cardiac death: a distinct clinical and electrocardiographic syndrome. A multicenter report*, J. Am. Coll. Cardiol., **20** (1992), no. 6, 1391-1396.
7. Bourgault, Y.; Coudière, Y.; Pierre, C. – *Existence and uniqueness of the solution for the bidomain model used in cardiac electrophysiology*, Nonlinear Anal. Real World Appl., **10** (2009), no. 1, 458-482.
8. Brugada, P.; Brugada, R.; Mont, L.; Rivero, M.; Geelen, P.; Brugada, J. – *Natural history of Brugada syndrome: the prognostic value of programmed electrical stimulation of the heart*, J. Cardiovasc. Electrophysiol., **14** (2003), no. 5, 455-457.
9. Bueno-Orovio, A.; Cherry, E.M.; Evans, S.J.; Fenton, F.H. – *Basis for the Induction of Tissue-Level Phase 2 Reentry as a Repolarization Disorder in the Brugada Syndrome*, BioMed Res. Int., 2015, 197586.
10. Clancy, C.E.; Rudy, Y. – *Na^+ Channel Mutation that causes both Brugada and Long-QT syndrome phenotypes*, Circulation, **105** (2002), no. 10, 1208-1213.
11. Colli Franzone, P.; Pavarino, L.F. – *A parallel solver for reaction-diffusion systems in computational electrocardiology*, Math. Models Methods Appl. Sci., **14** (2004), no. 6, 883-911.
12. Colli Franzone, P.; Pavarino, L.F.; Scacchi, S. – *Mathematical Cardiac Electrophysiology*, MS&A, Modeling, Simulation and Applications, Springer, Cham, **13** (2014).
13. Colli Franzone, P.; Pavarino, L.F.; Scacchi, S. – *A Numerical Study of Scalable Cardiac Electro-Mechanical Solvers on HPC Architectures*, Front. Physiol., **9** (2018), 268.

14. Colli Franzone, P.; Pavarino, L.F.; Taccardi, B. – *Simulating patterns of excitation, repolarization and action potential duration with cardiac bidomain and monodomain models*, Math. Biosci., **197** (2005), no. 1, 35-66.
15. Colli Franzone, P.; Savaré, G. – *Degenerate evolution systems modeling the cardiac electric field at micro and macroscopic level*, Evolution equations, semigroups and functional analysis, Milano, (2000), 4978, Progr. Nonlinear Differential Equations Appl., Birkhäuser, Basel, **50** (2002).
16. Geselowitz, D.B.; Miller, W.T. – *A bidomain model for anisotropic cardiac muscle*, Ann. Biomed. Engrg., **11** (1983), 191-206.
17. Hodgkin, A.L.; Huxley, A.F. – *A quantitative description of membrane current and its application to conduction and excitation in nerve*, J. Physiol., **117** (1952), no. 4, 500-544.
18. Hoogendijk, M.G.; Potse, M.; Vinet, A.; de Bakker, J.M.T.; Coronel, R. – *ST segment elevation by current-to-load mismatch: an experimental and computational study*, Heart Rhythm, **8** (2011), no. 1, 111-118.
19. Keener, J.; Sneyd, J. – *Mathematical physiology*, Interdisciplinary Applied Mathematics, Springer-Verlag, New York, **8** (1998).
20. Neu, J.C.; Krassowska, W. – *Homogenization of syncytial tissues*, Crit. Rev. Biomed. Engrg., **21** (1993), no. 2, 137-199.
21. Pappone, C.; Ciconte, G.; Manguso, F.; Vicedomini, G.; Mecarocci, V.; Conti, M.; Giannelli, L.; Pozzi, P.; Borrelli, V.; Menicanti, L.; Calovic, Z.; Della Ratta, G.; Brugada, J.; Santinelli, V. – *Assessing the Malignant Ventricular Arrhythmic Substrate in Patients with Brugada Syndrome*, J. Am. Coll. Cardiol., **71** (2018), no. 15, 1631-1646.
22. Pennacchio, M.; Savaré, G.; Colli Franzone, P. – *Multiscale modeling for the bioelectric activity of the heart*, SIAM J. Math. Anal., **37** (2005), no. 4, 1333-1370.
23. Quarteroni, A.; Valli, A. – *Numerical approximation of partial differential equations*, Springer Series in Computational Mathematics, Springer-Verlag, Berlin, **23** (1994).
24. Scacchi, S. – *A multilevel hybrid Newton-Krylov-Schwarz method for the bidomain model of electrocardiology*, Comput. Methods Appl. Mech. Engrg., **200** (2011), no. 5-8, 717-725.
25. ten Tusscher, K.H.W.J.; Noble, D.; Noble, P.J.; Panfilov, A.V. – *A model for human ventricular tissue*, Am. J. Physiol. Heart Circ. Physiol., **286** (2004), H1573-H1589.
26. ten Tusscher, K.H.W.J.; Panfilov, A.V. – *Alternans and spiral breakup in a human ventricular tissue model*, Am. J. Physiol. Heart Circ. Physiol., **291** (2006), H1088-H1100.
27. Tsumoto, K.; Ashihara, T.; Naito, N.; Shimamoto, T.; Amano, A.; Kurata, Y.; Kurachi, Y. – *Specific decreasing of Na+ channel expression on the lateral membrane of cardiomyocytes causes fatal arrhythmias in Brugada syndrome*, Sci Rep., **10** (2020), 19964.
28. Tung, L. – *A bi-domain model for describing ischemic myocardial D-C potentials*, Ph.D. dissertation, Massachusetts Institute of Technology, 1978.
29. Veneroni, M. – *Reaction-diffusion systems for the macroscopic bidomain model of the cardiac electric field*, Nonlinear Anal. Real World Appl., **10** (2009), no. 2, 849-868.
30. Vigmond, E.J.; Aguel, F.; Trayanova, N.A. – *Computational techniques for solving the bidomain equations in three dimensions*, IEEE Transactions on Biomedical Engineering, **49** (2002), no. 11, 1260-1269.
31. Xia, L.; Zhang, Y.; Lu, X.H. – *Cellular modeling and simulation of Brugada syndrome*, Computers in Cardiology, **32** (2005), 1001-1004.

Received: 14.XII.2020 / Accepted: 15.XII.2020

Authors

Silvia Caligari,
Dipartimento di Matematica,
Università degli Studi di Pavia,
Via Ferrata 1, 27100 Pavia, Italy,
E-mail: silvia.caligari01@universitadipavia.it

Simone Scacchi,
Dipartimento di Matematica,
Università degli Studi di Milano,
Via Saldini 50, 20133 Milano, Italy,
E-mail: simone.scacchi@unimi.it